Protecting the engine speed controller board of UAV against conducted UWB pulses

Alexander Kornev
Television and Control Departamet Tomsk State University of Control Systems and Radioelectronics
Tomsk, Russian Federation
kornev12333@mail.ru

Dmitriy Petukhov
Television and Control Departamet Tomsk State University of Control Systems and Radioelectronics
Tomsk, Russian Federation
dimasuper06@bk.ru

Anton Belousov
Television and Control Departamet Tomsk State University of Control Systems and Radioelectronics
Tomsk, Russian Federation
anton.belousov@tu.tusur.ru

***Abstract*— This work explores the possibility of applying modal filtration technology to protect the engine speed controller board of an unmanned aerial vehicle (UAV) from conducted ultra-wideband (UWB) pulses. The selection and justification of a specific UAV and its radio-electronic equipment are carried out. The main paths of UWB pulses propagation on the engine speed controller board are determined. Devices to protect the selected board from UWB pulses are proposed. Simulation and optimization (based on time and amplitude criteria) of modal filters (MF) are performed in quasi-static and electrodynamic analysis. Strip and cable structures are considered as MF. The simulation results demonstrate high efficiency of applying MFs to protect the engine speed controller board from UWB pulse excitation. As a result, UWB pulse with an EMF of 500 V and a total duration of 60 ps was attenuated from 44 times to 62 times. Finally, we developed MF prototypes suitable for use as part of UAVs to protect equipment against conducted UWB pulses.**

Keywords—modal filters, electromagnetic compatibility, unmanned aerial vehicle, engine speed controller, ultra-wideband pulses.

I. INTRODUCTION

With each passing year, modern radio-electronic equipment (REE) requires increasingly careful attention in terms of electromagnetic compatibility (EMC) [1]. This is explained by their rapid growth in terms of increasing operating frequencies, miniaturization, integration into various fields, and as a result, wide prevalence. However, the impact of electromagnetic interference (EMI) (both natural and artificial) can disrupt normal operation of REE. The general classification of EMI implies their division into two main types: radiated and conducted. The latter spread through conductors, and their sources can be current circuit switching, secondary effects of lightning discharge, electrostatic discharges, ultra-wideband (UWB) pulse, and others [2,3]. In addition, there is a growing trend towards the use of unmanned aerial vehicles (UAVs) in various sectors, including civilian applications (forestry, oil and gas industry, film industry, mapping, monitoring, and others), as well as military purposes. Many developed countries actively use UAVs for various military tasks, from observation and monitoring to combat operations, which underscores the importance and demand for UAVs [4].

In the meantime, the development of UWB pulse generators is actively underway. These generators can be represented by complex systems designed, among other things, for counteracting UAVs. A prominent example of such complexes is the EMI-based functional destruction system. The effectiveness of these systems directly depends on the knowledge of specific characteristics and elements of the REE comprising each UAV. Therefore, it is important to ensure the EMC of UAV REE, especially the equipment that may be within the damage area of the EMI-based functional destruction system. These distruction systems typically operate by emitting UWB pulses directionally within a specific radius. Such pulses are also known as ultrashort pulses (USP) with sub-nanosecond rise times and high voltage levels [6]. An example is the SINUS-200 radio pulse generator with a horn antenna, which generates pulses with 2.5 ns fronts, a total duration of 9 ns, and an amplitude of up to 290 kV on a 30 Ω load [7].

To protect REE from USPs, engineers are actively developing modal filters (MF) [8]. These are devices based on modal filtration technology that utilyzes the delays of modal propagation in the transmission line to decompose a USP into a sequence of pulses of lower amplitudes. Traditionally, MFs are implemented as strip structures on printed circuit boards; however, modal decomposition can also occur in cable structures. Such MFs have several advantages over printed circuit board (PCB) ones, for example, design flexibility, greater length, and the ability to use ready-made cables to protect REE against USPs [9]. When a UAV performing a combat mission enters the area affected by EMI-based functional destruction system, there is a high probability of significant malfunctions that can occur due to changes in electrophysical parameters of its semiconductor or optoelectronic elements. The application of MFs in UAVs in this case can provide proper UWB pulse suppression at minimal financial and mass-volume costs. Therefore, this work aims to comprehensively study the possibility of using strip and cable MFs in UAVs to protect against UWB pulses.

We propose to select a specific UAV, determine the REE in its configuration (as well as their maximum voltage levels), assess the paths of conducted interference propagation through the REE circuits, model and optimize MFs to reduce levels of UWB pulses propagating through the UAV circuits to an acceptable level.

The reported study was funded by the Russian Science Foundation, project number 24-29-00578.

II. Selection of Unmanned Aerial Vehicles and their Radio-Electronic Equipment

The selection of UAVs was carried out based on three main criteria: payload (weight that the UAV can lift without considering its own and that does not affect its flight characteristics), available space for mounting protection devices, and the availability of information about the UAV from open sources. First, we considered DJI Phantom 3, which has an assembled weight of 1216 g, and the maximum takeoff weight declared by the manufacturer is 1500 g. Thus, its payload is 284 g. However, the tight arrangement of electronic components inside the UAV complicates the installation of additional pulse protection devices without violating the manufacturer's declared UAV design. In addition, information about the electronic components in DJI Phantom 3 is hidden and not available for general use [10].

Next, we considered the Eachine Wizard X220 V3 FPV. The weight of this UAV is 358 g without a battery and 551 g with it, with a maximum takeoff weight of 740 g. Thus, the payload is 189 g [11]. It is worth noting that information about its REE components is openly available. The height of the central part of the UAV is 38 mm, the thickness of the beams is 5 mm, and the combined thickness of the lower and upper support plates is 6 mm. The height of the mounts for the flight controller and video-transmitter is 22 mm. Considering the above, the ability to use pulse suppression devices is limited.

Finally, we reviewed the Darwin 129 7" Long Range PNP UAV (hereinafter referred to as Darwin 129). Darwin 129 has several advantages compared to other rotary-type UAVs. It has a high payload capacity of 1.6 kg (with a total weight of 387.7 g), a suitable airframe size, and available space for mounting protective devices. The external appearance of Darwin 129 is presented in Fig. 1 [12].

Fig. 1. Darwin 129

Darwin 129 has dimensions of 280×280×74 mm. Its airframe is made of 3K carbon material (one bundle contains 3000 carbon fibers or filaments). The structure of the airframe allows installing protection devices on the beams, in the upper, lower, and central parts with proper placement of boards and manual adjustment of their mounting height (Fig. 2).

a

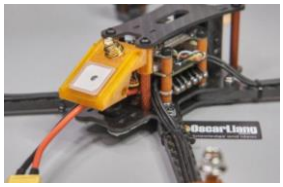

b

Fig. 2. Central (*a*) and rear (*b*) parts of Darwin 129

In the central part there is a flight controller, an engine speed controller, and a video-transmitter, stacked on top of each other with a 10 mm spacing. This provides additional space of about 17 mm for placing interference protection devices by offsetting the mentioned printed circuit boards. Table 1 summarizes the results of UAV selection based on the criteria listed above.

TABLE I. UAV Characteristics According to Selected Criteria

	DJI Phantom 3	***Eachine Wizard X220***	***Darwin 129***
Payload, g	284	189	1612
Price, rub	≈66526	≈18975	≈21233
Availability of information	No	Yes	No
Dimensions, mm	300×300×160	145×145×38	280×280×74
Available space	No	No	Yes

It can be seen that Darwin 129 stands out because of its large payload capacity compared to other models, which allows placing interference protection devices without compromising its flight and technical characteristics. Additionally, this UAV possesses a vast amount of accessible information. Fig. 3 shows the structural diagram of the UAV. There are key systems responsible for the direct fulfillment of the UAV mission: the flight controller and the engine speed controller. In this study, we investigate the engine speed controller PCB of the 4In1 50A Blheli S ESC engines within Darwin 129 (Fig. 4).

The engine speed controller is responsible for controlling the motor rotation speed. It ensures stable rotation speeds in different flight modes, allowing the UAV to maintain a certain velocity and maneuverability. This PCB model has 12 contacts (6 on each side) for connecting brushless motors 2507 1800KV 3-6S that have a maximum continuous power rating of 840 W and a current consumption of 42 A. Furthermore, at the bottom of the speed controller, there are two contacts for connecting the CNHL Black Series 1500 mAh battery and a power capacitor (on the reverse side). The engine speed controller is equipped with one port to connect with the flight controller. The main paths of conducted UWB pulse propagation on the engine speed controller PCB are shown in Fig. 5.

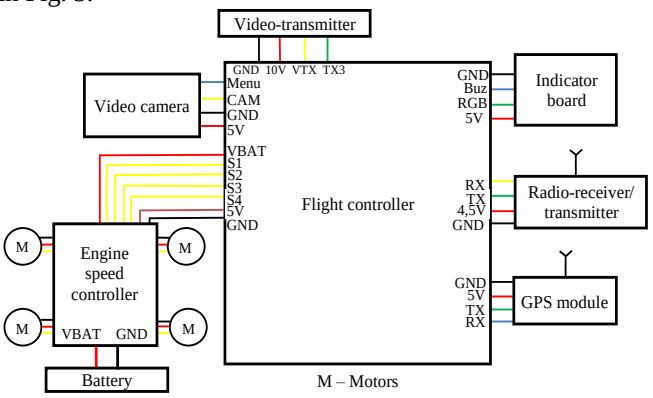

Fig. 3. Structural diagram of the Darwin 129 main systems

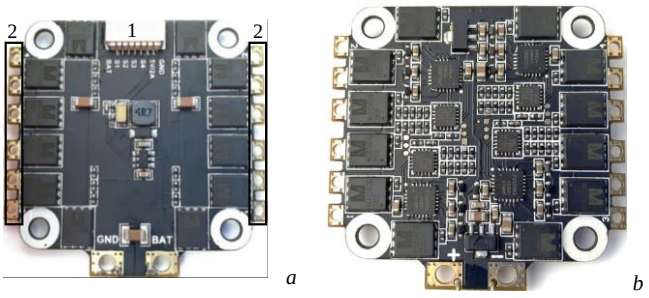

Fig. 4. External view of the engine speed controller: (*a*) top layer and (*b*) bottom layer.

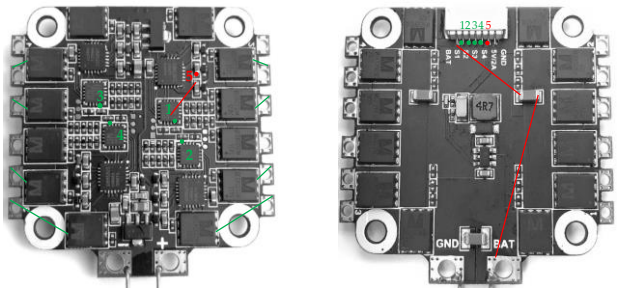

Fig. 5. The main paths of UWB pulse propagation in the engine speed controller, where (– and •) is a power supply circuit and (•) is a signal circuit

From Fig. 5, it can be seen that the first components connected to the ports for connecting various REE on the potential path of radiated UWB pulse are 4 identical EFM8BB21F16G microcontrollers. Their operating voltage is 3.3 V, and the maximum input voltage is 5.25 V. Tables 2 and 3 list the first components on the path of the UWB pulse along the power supply circuit and the signal circuit of the controller, along with their operating and maximum voltages.

TABLE II. FIRST COMPONENT OF THE ENGINE SPEED CONTROLLER IN THE PATH OF UWB PULSE PROPAGATION FROM PORT 1 (SPI)

Microcontroller EFM8BB21F16G	
Voltage, V	
Operating	***Maximum***
3.3	5.25

TABLE III. FIRST COMPONENT OF THE ENGINE SPEED CONTROLLER ON THE PATH OF UWB PULSE PROPAGATION FROM CONTACTS OF MOTOR CONNECTORS 2 THROUGH THE SIGNAL CIRCUIT AND POWER CIRCUIT

Transistor G2306	
Voltage, V	
Operating	***Maximum***
2	20

Through the analysis of the engine speed controller board, we propose a structural diagram of the REE that takes into account the use of an MF based on strip (MF_{PCB}) structure (Fig. 6). Additionally, to protect against the impact of UWB pulse, we suggest replacing the manufacturer-installed wires with a cable-based MF (MF_C) by adjusting the positioning of individual wires and/or consolidating them under a single insulation.

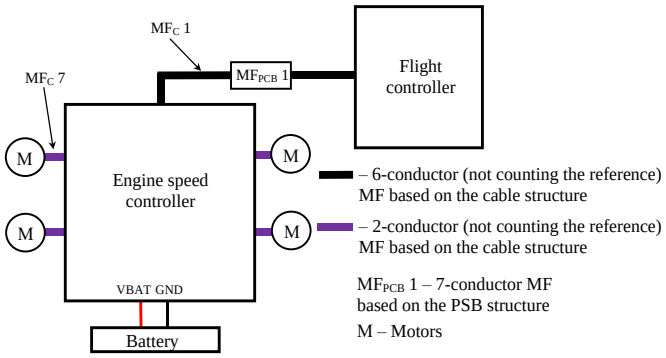

Fig. 6. Modernized structural diagram of Darwin 129

The modernized structural diagram involves the use of a 7-conductor microstrip MF (MF_{PCB} 1), 6- and 2-conductor MFs based on a cable structure (MF_C 1 and MF_C 7).

III. METHODS AND APPROACHES

Simulation was performed in systems of quasi-static and electrodynamic analyses. Using a quasi-static approach, only the propagation of transverse *T*-waves was considered, while higher types of waves were not taken into account. This approach can be used in simulating PCB lines, the transverse dimensions of which are small compared to the wavelength [13]. The reason is that the longitudinal components of the field intensity will be small compared to the transverse components [14]. The description of wave processes in the quasi-static approach is based on telegraph equations, to which Maxwell's equations are reduced. Solving these equations is less costly, and the accuracy provided by this approach is acceptable even for solving complex problems. This approach is implemented in the TALGAT software [15,16].

In the electrodynamic (full-wave) approach, all types of waves are taken into account, which allows increasing the calculation accuracy, but also leads to high computational costs, even when elementary configurations are simulated. Therefore, the electrodynamic approach is mainly used for simulating structures at high frequencies (tens and hundreds of GHz). When simulating and optimizing MF_{PCB}, it was important to obtain the resulting level of the interfering UWB pulse at the output, below the maximum value of the input voltage of the first component in the path of UWB pulse propagation.

The cross-section of a 7-conductor MF_{PCB} 1 is shown in Fig. 7, where w is the conductor width, s_i is the gap between the conductors, t is the conductor thickness, h is the substrate thickness, d is the distance from the edge of the MF to the nearest conductors of the MF, and ε_{ri} is the relative permittivity of the substrate. Geometrical parameters were optimized through heuristic search to reduce the level of UWB pulse at the output of MF_{PCB} 1. In addition, the equivalent circuit shown in Fig. 8, with loads at the ends of all conductors (R) set to 50 Ω and the line length (l) assumed to be 139 mm. As an excitation, we used a digitized UWB pulse with an EMF amplitude of 500 V, durations of rise, fall and flat top of 42 ps,

30 ps, and 4 ps (at levels 0.1–0.9), respectively, resulting in a total duration (at level 0.5) of 60 ps.

Fig. 7. Cross-section of MF_{PCB} 1

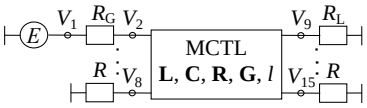

Fig. 8. Equivalent circuit of MF_{PCB} 1

In this study, MF_C flat cables are used for more convenient connection of REE. When simulating and optimizing the MF_C, the main goal was to obtain the resulting level of UWB pulse at the output of the cables below the maximum value of the voltage of the first component in the path of the UWB pulse propagation. The cross section of the 6-conductor MF_C 1(not including the reference conductor) is shown in Fig. 9*a*, where r_1 is the conductor radius, r_2 is the insulation radius around the conductors, r_3 is the outer insulation radius, and ε_{ri} is the relative permittivity of the substrate. Geometrical parameters optimization was performed through heuristic search to reduce the level of the UWB pulse at the output of the flat cables. The equivalent circuit is shown in Fig. 10*a*, where the *R* values are assumed to be 50 Ω, and *l*=50 mm. The parameters of the UWB pulse are the same as those used to simulate the MF_{PCB} 1. MF_C 1 is designed to replace the cable connecting the flight controller and the engine speed controller. Figs. 9*b* and 10*b* show the cross section and equivalent circuit of the 2-conductor MF_C 7 (not including the reference conductor). The *R* values are also assumed to be 50 Ω, and *l*=115 mm. MF_C 7 is designed to replace the wires connecting the engine speed controller board and the motors.

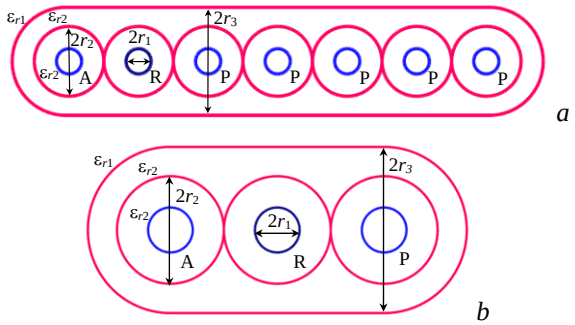

Fig. 9. Cross-section of a 6-conductor MF_C 1 (*a*) and a 2-conductor MF_C 7 (*b*)

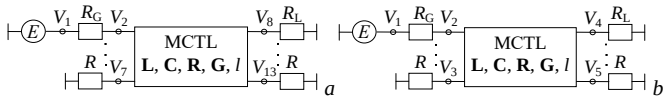

Fig. 10. Equivalent circuit of a 6-conductor MF_C 1 (*a*) and a 2-conductor MF_C 7 (*b*)

It is assumed that the required level of the UWB pulse attenuation will be achieved through the use of both an MF_{PCB} and an MF_C. The structure of MF 1 is a combination of sequentially connected MFs for maximum attenuation of the UWB pulse. It consists of two segments of MF_C 1 between which the MF_{PCB} 1 is located. Thus, it is assumed that the UWB pulse enters the input of the first segment of the MF_C, where it is subsequently attenuated. Next, the pulse enters the MF_{PCB} input, after which it passes to the second segment of the MF_C. Fig. 11 shows a generalized structural diagram of MF 1.

Fig. 11. Generalized schematics of series-connection of MF 1

IV. Simulation Results

This section presents the results of simulating the filters in quasi-static and electrodynamic analysis systems. The parameters obtained as a result of optimizing the cross-section of the MF_{PCB} 1 are the following: w=350 μm, s_1=165 μm, s_2=225 μm, s_3=370 μm, s_4=390 μm, s_5=410 μm, s_6=420 μm, h=200 μm, d=1050 μm, t=105 μm, and ε_{r1}=1. The substrate chosen is the composite material Arlon AD 1000 with a relative permittivity value ε_{r2}=10.2 and a loss tangent of tgδ=0.025 [17].

The geometric parameters of the MF_C 1cross-section were optimized in a similar way. The parameters resulting from the optimization are the following: r_1=0.4 mm, r_2=1.1 mm, r_3=2.4 mm, and ε_{r1}=1. RPM Zipsil 410 RPM-L was selected as insulation with a relative permittivity value of ε_{r2}=20, a tangent of the loss angle tgδ=0.36, and a relative magnetic permeability of μ=2.7. The MF_C 7cross section obtained as a result of optimization has the following geometric parameters: r_1=0.8 mm, r_2=1.5 mm, r_3=4.7 mm, ε_{r1}=1, and ε_{r2}=20.

A. *Modal filters based on a strip structure*

Fig. 12 shows the forms of EMF and voltages at the input and output of MF_{PCB} 1 obtained in quasi-static and electrodynamic analyses.

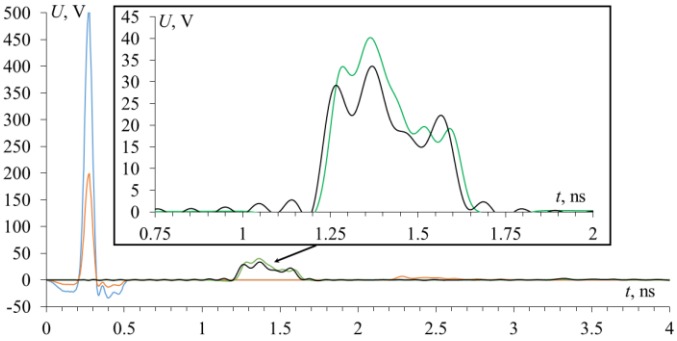

Fig. 12. Waveforms of EMF (–), voltages at the MF_{PCB} 1 input (–) and output during quasi-static (–) and electrodynamic (–) analyses

It can be seen from the figure that the mode delays and pulse forms in the simulations in the two systems are comparable to each other. The maximum voltage amplitude at the MF_{PCB} 1output, obtained in the electrodynamic analysis, is 33.64 V, which differs from the results of quasi-static analysis (40.22 V) by 16%. The difference can be explained by the

presence of radiation losses which are taken into account only during electrodynamic analysis. The attenuation of the excited UWB pulse is 6 times.

B. Modal filters based on a cable structure

This subsection presents the results of simulating MF_C in a system of quasi-static and electrodynamic analysis. The waveforms of EMF and voltages at the MF_C 1input and output are shown in Fig. 13.

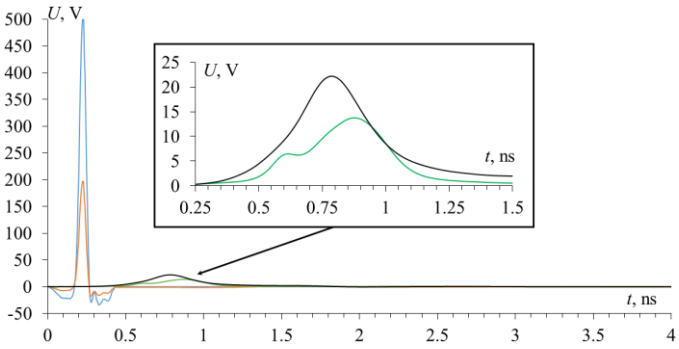

Fig. 13. Waveforms of EMF (–), voltages at the MF_C 1input (–) and output during quasi-static (–) and electrodynamic (–) analyses

It can be seen that the pulses arrive at the MF_C 1output at similar time points; however, there are differences in the maximum amplitudes of the decomposition pulses. Thus, the maximum output voltage of MF_C 1 obtained in the electrodynamic analysis is 22.19 V, whereas in the quasi–static analysis it is 13.76 V. Fig. 14 shows the waveforms of EMF and voltages at the MF_C 7 input and output. This MF, due to its length, can weaken the exciting UWB pulse to the desired level (no more than 20 V at the output), therefore MF_C 7 can be installed without additional MF_{PCB}.

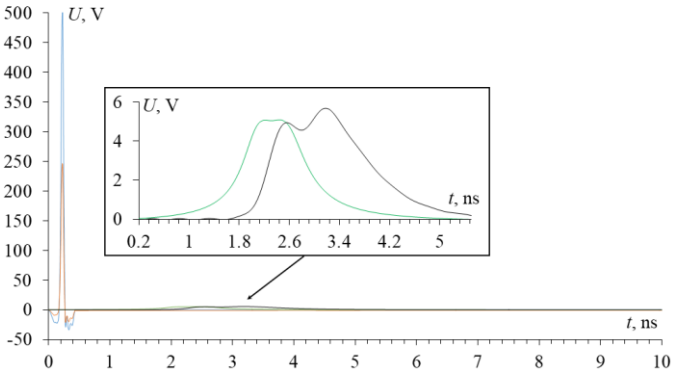

Fig. 14. Waveforms of EMF (–), voltages at the MF_C 7 input (–) and output during quasi-static (–) and electrodynamic (–) analyses

Simulations in the two systems demonstrate that the first decomposition pulses arrive at the MF_C 7output at different time points. This can be explained by the fact that the two systems consider the frequency dependence of ε_r in different ways. Meanwhile, the maximum amplitude of the pulses at the MF_C 7output, obtained as a result of electrodynamic analysis, is 5.69 V (attenuation is 44 times), which differs slightly from the results of quasi-static analysis (5.09 V).

C. Simulation of series-connected modal filters

Finally, we simulated MF 1 consisting of series-connected MF_C 1 (at the beginning and end) and MF_{PCB} 1. The waveforms of EMF and voltages at the input and output of the MF 1 obtained as a result of electrodynamic analysis are shown in Fig. 15.

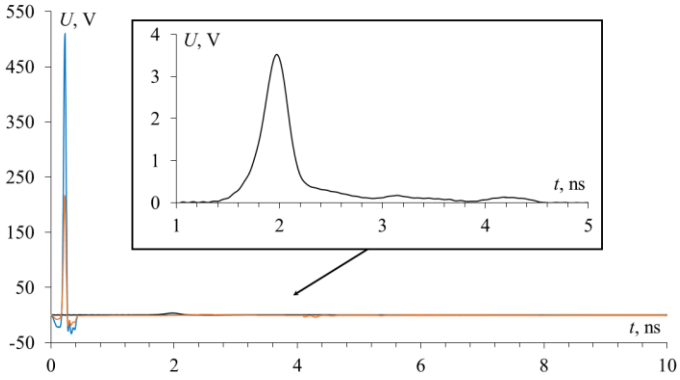

Fig. 15. Waveforms of EMF (–), voltage at the input (–) and output (–) of MF 1

It can be seen that pulses arrive at the MF 1output (which is a set of modes with similar time intervals between them) with a maximum amplitude of 3.54 V. Thus, the use of series-connected MF 1 allowed weakening the affecting UWB pulse by 62 times (compared with the input voltage of 220 V).

Tables 4 and 5 summarize the first components of the board in the path of the UWB pulse propagating along the signal and power supply circuits, as well as the maximum voltages of these components and the voltage obtained at the output of the proposed MF_C 7 and MF 1 (fed directly to the indicated components).

TABLE IV. FIRST COMPONENT OF THE ENGINE SPEED CONTROLLER IN THE PATH OF UWB PULSE PROPAGATION FROM PORT 1 THROUGH THE SIGNAL AND THE POWER SUPPLY CIRCUITS AND THE MF 1 OUTPUT VOLTAGE

Microcontroller EFM8BB21F16G	
Voltage, V	
Maximum	***Output MF 1***
5.25	3.54

TABLE V. FIRST COMPONENT OF THE ENGINE SPEED CONTROLLER IN THE PATH OF UWB PULSE PROPAGATION FROM THE MOTOR CONNECTION CONNECTORS 2 ALONG THE SIGNAL AND THE POWER SUPPLY CIRCUITS AND THE MF_C 7 OUTPUT VOLTAGE

Transistor G2306	
Voltage, V	
Maximum	***Output MF_C 7***
20	5.69

To place MFs in the UAV, we also traced the 7-conductor MF_{PCB} 1 in the electrodynamic analysis system. The initial dimensions of MF_{PCB} 1 were 139×6.55×0.305 mm. Due to proper layout, the final dimensions were reduced to 30.5×30.5×0.305 mm. The 3D model of the MF_{PCB} 1 prototype is shown in Fig. 16. It corresponds to the dimensions of the mounting holes of the flight controller and engine speed controller board.

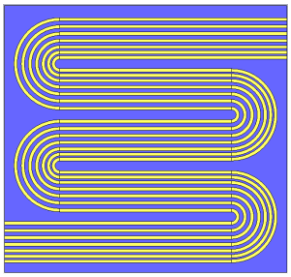

Fig. 16. 3D model of the MF_{PCB} 1 prototype

Fig. 17 shows the appearance of 3D models of the MF_C 1 and MF_C 7 prototypes. The sections of the original wires remained unchanged. This was done for the proposed cables to operate normally, while providing additional protection for the UAV REE from external UWB pulse.

a *b*

Fig. 17. 3D models of MF_C 1 (*a*) and MF_C 7 (*b*) prototypes

V. Conclusion

The paper considers the possibility of using MFs to protect REE and UAV systems from the excitation of conducted UWB pulse. The REE as part of the Darwin 129 UAV were analyzed. The PCB engine speed controller was detailed, i.e. the main components of the board and possible ways for a conducted UWB pulse to propagate along the power supply and signal circuit were determined. All MF structures were simulated in quasi-static and electrodynamic analysis systems. These structures included a strip structure based on a 7-conductor microstrip MF (MF_{PCB} 1), as well as 6- (MF_C 1) and 2-conductor (MF_C 7) cable structures (not counting the reference conductor). As a result of simulating the strip MF_{PCB} 1, the UWB pulse was reduced from 200 V to 33.64 V (with the electrodynamic approach) and to 40.22 V (with the quasi-static approach). MF_C 1, in turn, attenuated the UWB pulse from 215 V to 22.19 V and 13.76 V. MF_C 7 attenuated the UWB pulse from 250 V to 5.69 V and 5.09 V. The structure of the series-connected MF_C 1 (at the beginning and end) and MF_{PCB} 1 allowed weakening the UWB pulse from 220 V to 3.54 V.

In addition, we developed MF layouts that can be used in UAVs to protect REE against conducted UWB pulses. Finally, we elaborated the possibility of locating MF in the UAV by tracing them. This opens up the possibility of installing PCB MFs into the UAV. The next step will be to assess the integrity of the signals propagating through the UAV REE, taking into account the UWB pulse excitation. It also seems promising to comprehensively assess the impact of radiated emissions on the UAV airframe and its REE.

References

[1] R. Shishir, “Providing EMI protection and addressing EMC compatibility issues in a cognitive radio network,” 2016 International Conference on ElectroMagnetic Pulse & Compatibility (INCEMIC), Bengaluru, India, 2016, pp. 1–4.

[2] Bai J., Shi Y., Zhao G, “Research on electromagnetic pulse of vehicle GPS navigation equipment,” 2017 IEEE 5th Intern. Symposium on Electromagnetic Compatibility (EMC-Beijing). Beijing, China. 28–31 Oct. 2017. P. 1–5. doi: 10.1109/EMC-B.2017.8260366.

[3] H. Lee, K. Kim, J. Yousaf, W. Nah, J. Youn, D. Lee, C. Hwang, “Analysis of electromagnetic field pulse between an antenna and a multiple-noise source using active scattering parameters,” IEEE Intern. Symposium on Electromagnetic Compatibility & Signal, pp. 643–646, 07–11 Aug. 2017, doi: 10.1109/ISEMC.2017.8077947.

[4] S.I. Makarenko, Countering unmanned aerial vehicles, systems of control, communication and security, St.Peterburg, science-intensive technologies, 204 p., 2020.

[5] A.O. Belousov, “Approaches to ensuring electromagnetic compatibility of radioelectronic devices as part of a complex of functional destruction of unmanned aerial vehicles by powerful electromagnetic radiation,” no. 3, pp. 134-196, 2023, DOI: 10.24412/2410-9916-2023-3-134-196.

[6] A. T. Gazizov, A. M. Zabolotsky and T. R. Gazizov, “UWB Pulse Decomposition in Simple Printed Structures,” in IEEE Transactions on Electromagnetic Compatibility, vol. 58, no. 4, pp. 1136–1142, Aug. 2016.

[7] I.V. Romanchenko, “Generation of powerful nanosecond pulses of electromagnetic radiation based on lines with ferrite”, dis. candidate of Physical and Mathematical Sciences, Institute of High–current Electronics, Tomsk, Russia, pp. 157-160, 2019.

[8] T.R. Gazizov, A.M. Zabolotsky, “Modal decomposition of a pulse in segments of connected lines as a new principle of protection against short pulses,” no.4, pp. 40-44, 2006.

[9] A. O. Belousov and N. O. Vlasova, “Parametric optimization of the cables with the modal filtration effect,” Journal of Physics: conference Series, vol. 1862, no. 1, pp. 1–6, 2021.

[10] DJI Phantom 3, “DJI Phantom 3 overview, specifications, instructions,” [Online]. Available: https://dronnews.ru/obzory/dji/dji-phantom-3-standard.html [Accessed: February 8, 2024].

[11] Eachine Wizard X220 V3 FPV, “Review FPV Drone Eachine Wizard X220 V3,” [Online]. Available: https://oscarliang.com/eachine-wizard-x220-v3/ [Accessed: February 10 2024].

[12] Darwin 129 7" Long Range PNP, “Darwin 129 7" Long Range PNP overview, characteristics,” [Online]. Available: https://darwinfpv.com/products/darwin129-7-long-range-pnp [Accessed: February 12, 2024].

[13] J.D. Jackson, Classical electrodynamics, Wiley & Sons, New York, 641 p., 1962.

[14] A.R. Djordjevic, T.K. Sarkar and R.F. Harrington “Time–domain response of multiconductor transmission lines,” IEEE Proceedings, vol. 75, no. 6, P. 743–764, June 1987, doi: 10.1109/proc.1987.13797.

[15] S.P. Kuksenko, A.M. Zabolotsky, A.O. Melkozerov and T.R. Gazizov, “New possibilities of the TALGAT electromagnetic compatibility simulation system,” vol. 36, no. 2(36), June 2015, pp. 45-50.

[16] S. P. Kuksenko, “Preliminary results of TUSUR university project for design of spacecraft power distribution network: EMC simulation,” IOP Conf. Series: Materials Science and Engineering, Vol. 560. No. 012110, pp. 1–7, 2019.

[17] A.O. Belousov, A.V. Medvedev, E.B. Chernikova, T.R. Gazizov and A.M. Zabolotsky, “Switching Order after Failures in Symmetric Protective Electrical Circuits with Triple Modal Reservation,” vol. 13(6), No. 1074, June 2021, DOI: 10.3390/sym13061074.